Near-Field Microwave Imaging Antenna Array for Inline Intrusion Detection of Processed Products

(Article begins on next page)

Near-Field Microwave Imaging Antenna Array for Inline Intrusion Detection of Processed Products

Calin Ion Maraloiu*, Juan Felipe González-Pardo*, Jorge Alberto Tobon Vasquez§, Marco Ricci§, Francesca Vipiana*

*Department of Electronics and Telecommunications, Politecnico di Torino, 10129 Torino, Italy, calin.maraloiu@polito.it

§Wavision srl, Torino, Italy, jorge.tobon@wavision.it

***Abstract*—The presence of foreign bodies in packaged products can be assessed exploiting inline microwave imaging (MWI) inspection systems. The purpose is to illustrate an insight of the product's composition according to the dielectric properties of its constituents, by processing the scattering parameters of an array of antennas. This allows to unveil the position and shape of any potential extraneous material, with the advantage of a non-invasive, non-destructive and real-time testing. While the resulting dielectric contrast reconstructions depict a visual and qualitative overview of the analyzed item, quantitative metrics are essential to objectively evaluate their outcome. In this paper, we exploit size, overlap and boundary metrics to investigate the performances of a MWI system, made of an array of extended gap ridged slotted horn antennas, in locating a glass sphere, placed inside a commercial cocoa-spread jar, all numerically modeled.**

***Index Terms*—Food safety, industrial control, microwave imaging, microwave propagation, multi-frequency, non-invasive diagnostics.**

I. Introduction

Contamination monitoring is an assessment procedure that food and beverage industries enforce to guarantee the standards of the products and safeguard the health of the customers from hazards, such as plastic, glass or other unintentional fragments. Compared to currently deployed technologies, microwave imaging is a newer approach in the industrial context [1], [2], [3]. This technology is capable of providing volumetric images of the content of the inspected items, through non-ionizing screening, unlike x-ray machines. Moreover, MWI systems are not limited by the contaminant material type, as in the case of metal detectors. Microwave propagation is affected by the dielectric properties of the media. Materials, whose dielectric properties are different with respect to the background medium, alter the electromagnetic signals delivered and gathered by an antenna array. This principle can be exploited in different fields, for instance, in medical applications for pathologies detection [4], in the industrial context for material or defects' inspection [5], and for the evaluation of hidden or embedded objects [6].

Additionally, the setup of a MWI system is generally cost-effective: it typically consists of an array of antennas, connected to a vector network analyzer (VNA) and a processing unit. Accounting for the properties of the considered product and the industrial constraints, microwave imaging units are designed to provide a geometrical coverage of the investigation domain, ensure an adequate penetration depth and offer a good resolution of the targeted contaminants. MWI systems sample the scattering matrices associated with the uncontaminated and contaminated scenarios. Through an inversion procedure, it is possible to display the contrast map, which reconstructs a qualitative frame of the product composition and locates the presence of scatterers. This approach is very intuitive, since the outcome of the algorithm can be visually assessed and compared with the expected shape and position of the contaminant. However, a qualitative overview might not be enough to generalize and validate the performances and accuracy of a MWI system. Hence, the necessity of quantitative methods to analyze image quality, with the perspective of exploiting these results as reference for further improvement and optimization.

In this paper, we propose a MWI system, based on a set of six extended gap ridged slotted horn (EGRSH) antennas, arranged in an arch-shaped configuration, for inline inspection of packaged food products. In addition, we adopt metrics, conventionally exploited for medical imaging, to validate its capabilities. The case of study is a 3 mm radius glass sphere, placed inside a commercial cocoa-spread jar, in different locations. The methods are here applied on data obtained from multi-position and multi-frequency simulations, which replicate the industrial scenario of moving processing items.

II. MWI System Design

The proposed system and the product under inspection are reported in Fig. 1(a). The system integrates a set of six antennas placed in an arch configuration, screening the product in motion along the x-axis. The absence of antennas over the moving direction can generate elongated shaped patterns in the reconstructed contrast maps [7], given the restriction of placing antennas facing the jar. To address this problem, multiple spatial acquisitions are exploited, while the product is moving through the arch, to compensate for the otherwise poor coverage in its front and back portions. We propose a multi-position scenario, in which the jar is placed in five uniformly spaced positions over the x-direction, with a displacement of $\pm 2\,\mathrm{cm}$ with respect to the central point of the antenna array. The antenna is a compact $43 \times 40 \times 41\,\mathrm{mm}$ extended gap ridged slotted horn [8], which has been designed to operate in the frequency range $6 - 11\,\mathrm{GHz}$, providing an appropriate penetration and spatial resolution in the product under test [7]. The physical dimensions of the test container are detailed in

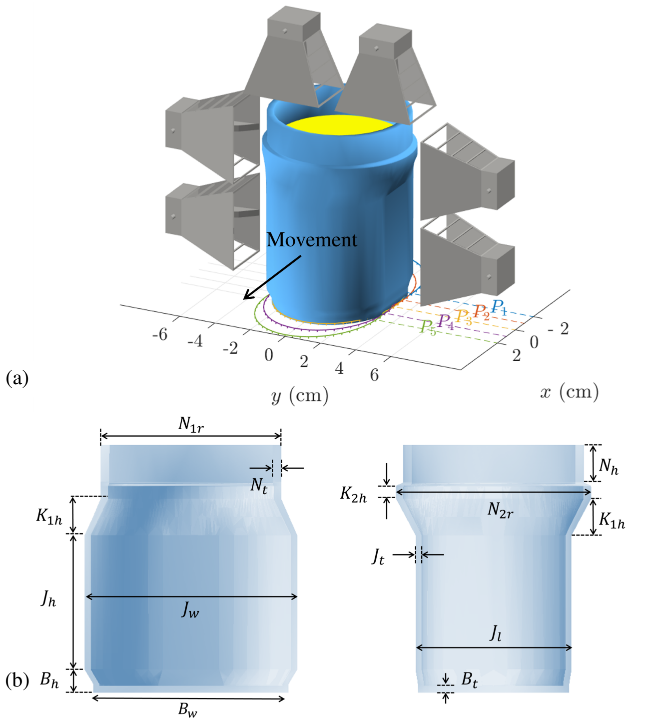

Fig. 1. (a): Proposed MWI setup including the six EGRSH antennas, disposed in an arch-shaped configuration around the inspected product and the proposed movement along the x-axis. (b): Model of the product under test.

Fig. 1(b) and summarized in Table I. This package is designed based on conventional commercial glass jars used to pack cocoa-based products. As in [9], the jar is filled with oil, whose dielectric properties are very similar to the cocoa cream. The proposed model accurately replicates the realistic scenario, minimizing the discrepancy between the model and the experimental setup. Figure 2 shows the average magnitude of the electric field at 6 and 11 GHz over the symmetry axes, when the product under test is in the central position. We can observe that the proposed setup provides a good field coverage inside the jar: the lower field, close to the jar borders, is compensated by the different jar positions with respect to the antenna arch.

TABLE I
DIMENSIONS OF THE TEST CONTAINER

Name	(cm)	Name	(cm)	Name	(cm)
J_w	8.70	J_h	5.50	J_l	6.40
N_{1r}	7.40	N_h	1.70	$N_t = B_t$	0.34
N_{2r}	8.00	B_w	8.20	J_t	0.23
B_h	1.00	K_{1h}	1.70	K_{2h}	0.40

III. PROBLEM FORMULATION

A. Microwave Imaging principle

Considering the setup shown in Fig. 1, the objective of the performed analysis is to evaluate the accuracy of the 3D qualitative dielectric contrast distributions of the investigated

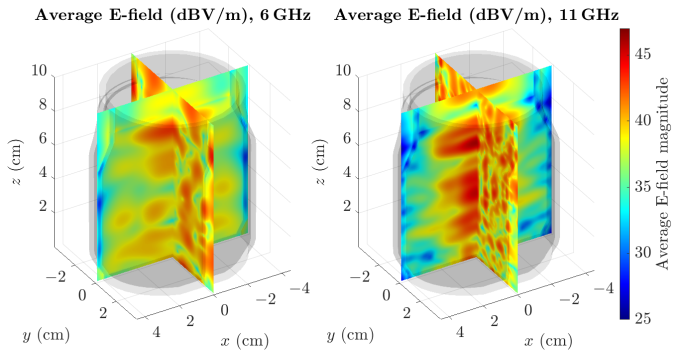

Fig. 2. Electric field distribution over the symmetry axes of the product under test at 6 and 11 GHz.

product, characterized by a complex background permittivity ϵ_b. The output data is the dielectric contrast, $\Delta\chi(\mathbf{r})$, which corresponds to the difference of the complex permittivity $\epsilon(\mathbf{r})$ and ϵ_b, then normalized to ϵ_b. The input data is the differential scattering matrix ΔS, derived by subtracting the scattering matrix of the scenario under test from that of the reference scenario (that is an uncontaminated jar filled with the background medium only). The discrete formulation of the linearized forward imaging principle, considering the distorted Born approximation, can be expressed by means of a system in a compact form:

$$[\Delta S] = [L][\Delta\chi], \tag{1}$$

where $[\Delta\chi]$ is the discretized dielectric contrast, and $[L]$ is the kernel mapping the contrast space into the data space. As shown in Fig. 1, we consider a multi-position scenario. Therefore, $[\Delta S]$ is formed through the vectorized concatenation of the scattering matrices associated with each P position. Given the set of transmitting and receiving antennas, and calling p and q any incoming and outgoing port of this system, the entries of $[L]$ can be computed as:

$$L_{(pq),n} = -\frac{j\omega\epsilon_b}{2a_p a_q}[\mathbf{E}_b(\mathbf{r}_p, \mathbf{r}_n) \cdot \mathbf{E}_b(\mathbf{r}_n, \mathbf{r}_q)]\Delta V_n, \tag{2}$$

where ω is the angular frequency, j is the imaginary unit, a_p and a_q are the root power waves at the p and q antenna ports, respectively. Each $L_{(pq),n}$ element is evaluated at the volume point $\mathbf{r}_n$ corresponding to the n-th mesh cell of volume ΔV_n, and depends on the background (unperturbed) electric fields $\mathbf{E}_b(\mathbf{r}_p, \mathbf{r}_n)$ and $\mathbf{E}_b(\mathbf{r}_q, \mathbf{r}_n)$, associated with the transmitting and receiving transceivers, respectively. Therefore, each row of the $[L]$ corresponds to a (p, q) pair of antennas at one of the five P shifts considered. On the other side, each column n is associated with a cell of the mesh.

The capability of $[L]$ to reconstruct accurate 3D maps depends mainly on the configuration, fields' distribution of the antennas, material properties and tested product. Choosing a multi-position approach improves the spatial coverage of the product. Indeed, spurious or ghost reconstructions of the scatterer, with no real physical correspondence, are a common problem caused by the intrinsic limitations of the $[L]$ kernel bases. Therefore, we exploit a multi-frequency strategy and the system stated in (1) can be reformulated in a block structure:

$$[\Delta S^F] = [L^F][\Delta\chi^M], \tag{3}$$

where $[\Delta\chi^M]$ is the multi-frequency dielectric contrast distribution [10]. The data vector is obtained by stacking the contributions from all F frequencies:

$$[\Delta S^F] = [\Delta S_1 \ \Delta S_2 \ \dots \ \Delta S_f \ \dots \ \Delta S_F]^{\mathrm{T}}, \tag{4}$$

with each $[\Delta S_f]$ corresponding to the differential scattering data at the f-th frequency. Similarly, the multi-frequency kernel is organized as

$$[L^F] = [L_1 \ L_2 \ \dots \ L_f \ \dots \ L_F], \tag{5}$$

where each block L_f represents the linear operator associated with the f-th frequency. This block formulation allows the combination of the single-frequency terms in one inversion procedure. Owing to the ill-posed nature of $[L^F]$, the system in (3) is solved by employing a truncated singular value decomposition (TSVD) [11]. Specifically,

$$[\Delta\chi^M] = \sum_{t=1}^{T} \frac{1}{\sigma_t} \langle [\Delta S^F], [u_t] \rangle [v_t], \tag{6}$$

denoting σ_t as the t-th singular value, while $[u_t]$ and $[v_t]$ represent the corresponding left and right singular vectors, respectively. The truncation index T sets the number of retained singular values, thereby defining the effective rank of the reconstructed approximation.

B. Quantitative metrics estimation

The outcome of (6) is a volumetric dielectric contrast distribution, and provides a qualitative representation of the detected scatterer within the product under test. In this framework, quantitative metrics are necessary to consistently appraise the quality of the obtained 3D map. As reported in [12], [13], [14], [15], in image segmentation there are mainly three viable approaches: overlap, size and boundary-based metrics. For our analysis, we explore a cartesian grid, discretizing the volume of the investigated jar in 1 mm edge cubic voxels. We call A the set of foreground voxels associated with the expected scatterer (ground truth) and B the set of foreground voxels associated with the reconstructed scatterer (prediction).

The first approach consists of estimating the overlap between A and B, through the dice similarity coefficient, namely:

$$\mathrm{DSC}(A,B) = \frac{2|A \cap B|}{|A| + |B|}, \tag{7}$$

where $|A \cap B|$ represents the number of shared voxels between the two sets, while $|A|$ and $|B|$ are their cardinalities. The $\mathrm{DSC}(A,B)$ ranges between 0 and 1, indicating a complete mismatch or a perfect overlap, respectively. This metric is effective in assessing the overlap, but totally insensitive to the shape of the reconstructed pattern and to the overall shift between the mismatched elements.

Instead, the second group of methods evaluates the size congruence. A viable strategy, proposed in [12], consists in evaluating the volume similarity (VS) parameter defined as:

$$\mathrm{VS}(A,B) = 1 - \frac{\big||A| - |B|\big|}{|A| + |B|}. \tag{8}$$

Identically, a perfect volume agreement is realized when VS = 1, while VS = 0 indicates incongruity between A and B. The metric effectively compares the predicted and ground-truth volumes, but its main limitation is the neglect of spatial alignment.

The third category of methods comprises boundary-based metrics, quantifying the distance between the contours defined by the volumes of A and B. An indication of the worst-case boundary error is provided by the Hausdorff distance (HD), which measures the largest minimum distance between the boundary points of A and B. Particularly, we employ a more robust variant, called 95th percentile Hausdorff distance (HD_{95}). Considering ∂A and ∂B the sets of boundary voxels of A and B, respectively, for each boundary voxel $a \in \partial A$, we define its distance to ∂B as:

$$d(a, \partial B) = \min_{b \in \partial B} \|\mathbf{r}(a) - \mathbf{r}(b)\|_2, \tag{9}$$

and for each boundary voxel $b \in \partial B$, we define its distance to ∂A as:

$$d(b, \partial A) = \min_{a \in \partial A} \|\mathbf{r}(b) - \mathbf{r}(a)\|_2, \tag{10}$$

where $\mathbf{r}(a)$, $\mathbf{r}(b)$ denote the coordinates of a and b, correspondingly. Therefore, the $\mathrm{HD}_{95}(A,B)$ is defined as:

$$\mathrm{HD}_{95}(A,B) = \max\left\{P_{95}(d(a,\partial B)),\ P_{95}(d(b,\partial A))\right\}, \tag{11}$$

where $P_{95}(\cdot)$ denotes the 95th percentile. This metric is not effective in estimating volume size or overlap agreement. Consequently, it is considered a complementary parameter to the previously described metrics.

IV. Numerical Validation of the Results

Figure 3 shows the five selected locations, for contaminants within the jar, that we explore as ground truth to test the

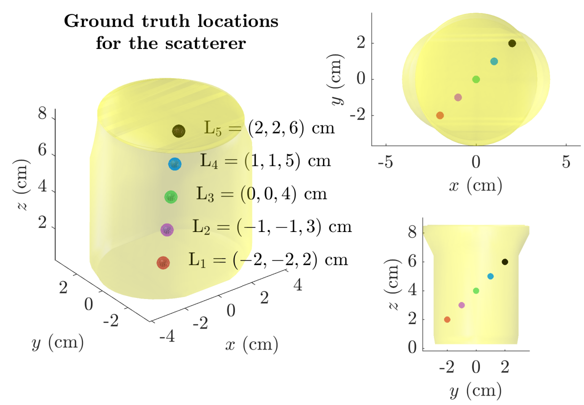

Fig. 3. Ground truth of the tested locations

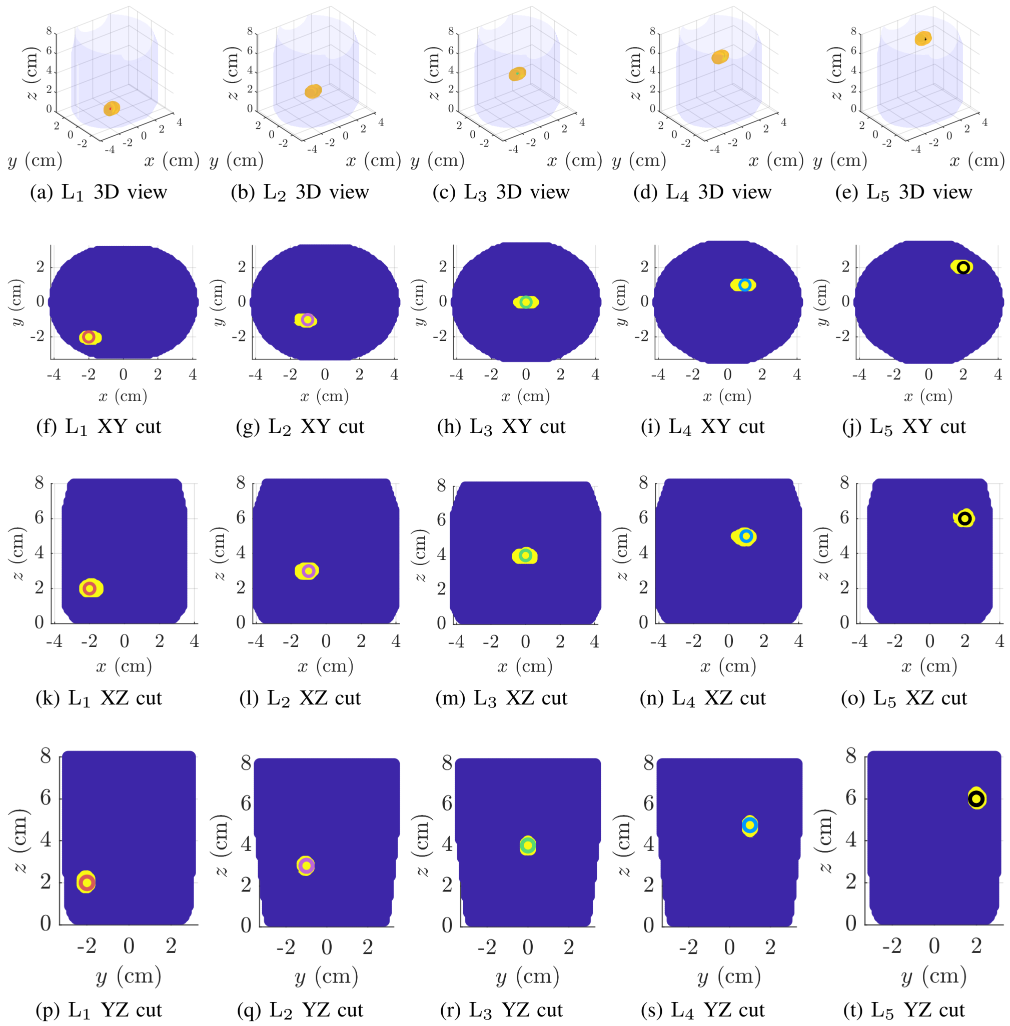

Fig. 4. Qualitative maps of the amplitude of the binarized contrast for the five tested positions: the colored spheres/circles represent the ground truth A, while the yellow locations correspond the contamination prediction B. The blue regions identify low contrast values zones, where no contamination is detected.

designed system performance and the different metrics. The performed simulations retrieve the scattering matrices, for both reference and contaminated scenarios at each scatterer location, necessary to compute $[\Delta\chi^M]$ in (6). Considering the binary representation required for contamination mapping (1 for the contaminated voxels and 0 otherwise), we fix the threshold for the amplitude of $[\Delta\chi^M]$ at 85 % of its maximum: the voxels with values above are set to 1 (high contrast) while the others are set to 0 (no contrast). Figure 4 reports the qualitative binarized maps. We can observe that the reconstructed dielectric contrast is very close to the ground truth: exploiting a multi-position configuration allows to focus the shape in the x-direction, and deploying a multi-frequency approach facilitates the suppression of possible artifact reconstructions, which are strongly dispersive. Moreover, the size and shape of the contaminant are visually matched for every tested position.

Table II summarizes the outcome of the metrics reported in Sect. III-B, applied to the results shown in Fig. 4. The number of predicted voxels $|B|$ is close to the ones of the ground truth $|A|$. The DSC(A, B) is relatively high, indicating a good overlap among the expected and detected scatterer, while the VS(A, B) reveals an excellent similarity in size. On the other hand, the HD$_{95}(A, B)$ indicates that the worst-case boundary error is of the order of 2 mm. These results prove that the adopted setup is suitable in locating the contaminant with high accuracy. The obtained results are also attributable to the lack of ghost reconstructions, known to adversely influence

TABLE II
QUANTITATIVE ASSESSMENT OF THE 3D RECONSTRUCTIONS

Assessment	L_1	L_2	L_3	L_4	L_5
$\lvert A\rvert$ (voxel)	123	123	123	123	123
$\lvert B\rvert$ (voxel)	125	110	103	117	126
DSC(A, B)	0.67	0.64	0.58	0.58	0.68
VS(A, B)	0.99	0.94	0.91	0.98	0.99
HD$_{95}(A, B)$ (mm)	2.00	2.24	2.00	2.24	2.00

the quantitative evaluation of the maps.

V. Conclusion and Perspectives

In this work, we presented a MWI system, consisting of an arch-shaped configuration of six EGRSH antennas, applied to inline food inspection, and a quantitative evaluation of the reconstructed volumetric contrast maps. The proposed analysis provides an assessment of the quality of the obtained reconstruction patterns. In addition, the results analyze the outcome of the MWI algorithm from an overlap, size and boundary perspective, for the considered setup. This study highlights the enhancements obtained through the use of EGRSH antennas and detailed modeling of the target product, in a simulation scenario.

Considering the promising results, further investigations will be performed for the practical study of this configuration and experimental testing.

Acknowledgment

This work is part of the project PNRR-NGEU which has received funding from the MUR – DM 117/2023. This research is supported in part by the project “INSIGHTFOOD – An innovative microwave sensing system for the evaluation and monitoring of food quality and safety”, funded by the Italian Ministry of Foreign Affairs and International Cooperation (MAECI, CUP E13C23000180005).

Furthermore, the authors are grateful to Dr. Lorenzo Crocco (CNR, IREA, Italy) for his expertise and valuable guidance in the design of the system.

References

[1] J. A. Tobon Vasquez, R. Scapaticci, G. Turvani, M. Ricci, L. Farina, A. Litman, M. R. Casu, L. Crocco, and F. Vipiana, “Noninvasive inline food inspection via microwave imaging technology: An application example in the food industry,” *IEEE Antennas and Propagation Magazine*, vol. 62, no. 5, pp. 18–32, 2020.

[2] M. Jelali and K. Papadopoulos, “Inline inspection of packaged food using microwave/terahertz sensing—an overview with focus on confectionery products,” *MDPI Processes*, vol. 12, pp. 1–21, 2024.

[3] F. Vipiana, L. Crocco, and J. LoVetri, “Electromagnetic imaging and sensing for food quality and safety assessment [guest editorial],” *IEEE Antennas and Propagation Magazine*, vol. 62, no. 5, pp. 16–17, 2020.

[4] C. Origlia, D. O. Rodriguez-Duarte, J. A. Tobon Vasquez, J.-C. Bolomey, and F. Vipiana, “Review of microwave near-field sensing and imaging devices in medical applications,” *Sensors*, vol. 24, no. 14, 2024. [Online]. Available: https://www.mdpi.com/1424-8220/24/14/4515

[5] J. LoVetri, M. Asefi, C. Gilmore, and I. Jeffrey, “Innovations in electromagnetic imaging technology: The stored-grain-monitoring case,” *IEEE Antennas and Propagation Magazine*, vol. 62, no. 5, pp. 33–42, 2020.

[6] W. Shao and T. McCollough, “Advances in microwave near-field imaging: Prototypes, systems, and applications,” *IEEE Microwave Magazine*, vol. 21, no. 5, pp. 94–119, 2020.

[7] M. Ricci, J. A. T. Vasquez, R. Scapaticci, L. Crocco, and F. Vipiana, “Multi-antenna system for in-line food imaging at microwave frequencies,” *IEEE Transactions on Antennas and Propagation*, vol. 70, no. 8, pp. 7094–7105, 2022.

[8] J. F. González-Pardo, C. I. Maraloiu, J. A. T. Vasquez, M. Ricci, and F. Vipiana, “UWB horn antenna for food inspection via microwave imaging,” in *2025 URSI International Symposium on Electromagnetic Theory (EMTS)*, 2025, pp. 1–4.

[9] A. Darwish, M. Ricci, J. A. T. Vasquez, C. Migliaccio, and F. Vipiana, “Near-field microwave sensing technology enhanced with machine learning for the non-destructive evaluation of packaged food and beverage products,” *Scientific Reports*, vol. 14, no. 1, p. 13413, 2024. [Online]. Available: https://doi.org/10.1038/s41598-024-62287-6

[10] C. I. Maraloiu, J. A. T. Vasquez, M. Ricci, L. Crocco, and F. Vipiana, “Multi-frequency microwave imaging inspection for industrial food quality assessment,” in *2025 19th European Conference on Antennas and Propagation (EuCAP)*, 2025, pp. 1–4.

[11] M. Bertero, P. Boccacci, and C. De Mol, *Introduction to inverse problems in imaging*. CRC press, 2021.

[12] A. A. Taha and A. Hanbury, “Metrics for evaluating 3D medical image segmentation: Analysis, selection, and tool,” *BMC Medical Imaging*, vol. 15, p. 29, 2015. [Online]. Available: https://bmcmedimaging.biomedcentral.com/articles/10.1186/s12880-015-0068-x

[13] F. Xue, L. Guo, A. Bialkowski, and A. M. Abbosh, “Integrated boundary-overlap-size metric for local assessment of deep learning methods in medical microwave imaging,” *IEEE Journal of Electromagnetics, RF and Microwaves in Medicine and Biology*, vol. 9, no. 2, pp. 229–239, 2025.

[14] R. Cárdenes, R. de Luis-García, and M. Bach-Cuadra, “A multidimensional segmentation evaluation for medical image data,” *Computer Methods and Programs in Biomedicine*, vol. 96, no. 2, pp. 108–124, 2009. [Online]. Available: https://www.sciencedirect.com/science/article/pii/S0169260709001424

[15] A. R. Reddy, E. V. Prasad, and L. S. S. Reddy, “Abnormality detection of brain MR image segmentation using iterative conditional mode algorithm,” *International Journal of Applied Information Systems*, vol. 5, no. 2, pp. 56–66, January 2013. [Online]. Available: https://www.ijais.org/archives/volume5/number2/421-0767/